1

JANUARY - MARCH

2015

ISSN 0024-998X

Magneto-Hydro-Dynamics

MAGNETOHYDRODYNAMICS Vol. 51 (2015), No. 1, pp. 177–178

INDEX

Baake E. *See*
Geza V., Nacke B., Baake E., Jakovičs A.;
Spitans S., Baake E., Nacke B., Jakovičs A.

Baltaretu F., Wang J., Letout S., Ren Z.M., Li X., Budenkova O., Fautrelle Y. Thermoelectric effects on electrically conducting particles in liquid metal, 45–56

Barglik J., Golak S. Modelling of filling a mold with molten metal in the presence of an electromagnetic field, 5–14

Ben-David O. *See*
Mikhailovich B., Ben-David O., Levy A.

Budenkova O. *See*
Baltaretu F., Wang J., Letout S., Ren Z.M., Li X., Budenkova O., Fautrelle Y.

Cramer A., Galindo V., Zennaro M. Frequency dependence of an alternating magnetic field driven flow, 133–148

Demidovich V. *See*
Minakov A., Khatsayuk M., Demidovich V., Pervukhin M.

Driesen J. *See*
Mirhoseini S.M.H., Van Reusel K., Driesen J.

Dropka N., Frank-Rotsch Ch. Enhanced VGF growth of single- and multicrystalline semiconductors using pulsed TMF, 149–156

Fautrelle Y. *See*
Baltaretu F., Wang J., Letout S., Ren Z.M., Li X., Budenkova O., Fautrelle Y.

Frank-Rotsch Ch. *See*
Dropka N., Frank-Rotsch Ch.

Galindo V. *See*
Cramer A., Galindo V., Zennaro M.

Geža V., Nacke B., Baake E., Jakovičs A. Anisotropy of flow and transition between mixing regimes in physical model of directional solidification, 15–24;
Ščepanskis M., Koroteeva E.Yu., Geža V., Jakovičs A.

Golak S. *See*
Barglik J., Golak S.

Jakovičs A. *See*
Geža V., Nacke B., Baake E., Jakovičs A.;
Pavlovs S., Jakovičs A., Sushkovs V., Nacke B.;
Spitans S., Baake E., Nacke B., Jakovičs A.;
Ščepanskis M., Koroteeva E.Yu., Geža V., Jakovičs A.

Khalilov R., Kolesnichenko I.. Annular linear induction pump for liquid sodium, 95–104

Khatsayuk M. *See*
Minakov A., Khatsayuk M., Demidovich V., Pervukhin M.

Kolesnichenko I. *See*
Khalilov R., Kolesnichenko I.

Koroteeva E.Yu. *See*
Ščepanskis M., Koroteeva E.Yu., Geža V., Jakovičs A.

Krauze A. *See*

MAGNETOHYDRODYNAMICS Vol. 51 (2015), No. 1, pp. 15–24

ANISOTROPY OF FLOW AND TRANSITION BETWEEN MIXING REGIMES IN A PHYSICAL MODEL OF DIRECTIONAL SOLIDIFICATION

V. Geža[1,2], *B. Nacke*[1], *E. Baake*[1], *A. Jakovičs*[2]

[1] *Institute of Electrotechnology, Leibniz University of Hannover*
[2] *Laboratory for Mathematical Modelling of Environmental and Technological Processes, University of Latvia*

This paper aims to provide an insight into the aspects of turbulence anisotropy in the directional solidification (DS) method, which is widely used for the growth of photo-voltaic silicon. In DS crucibles, the melt flow is usually stratified due to strong temperature gradients and this leads to anisotropy of flow and turbulence, which is often neglected in turbulence models used in engineering applications. In experimental measurements, a transition between strong and weak mixing regimes is found. The numerical simulations results provide quantitative measures for anisotropy and vertical heat transfer intensity within the range of different Richardson numbers (0.1 – 40).

Introduction. As fossil energy resources are getting exhausted, the demand for alternative energy sources is growing. In 2013 in Germany the renewable energy part was 29%, which has been doubled since 2006 [1]. Photo-voltaic solar energy still has a small fraction of the total power production, only 5.7%, but it keeps growing. Directional solidification (DS) is a widely used technique for the production of photo-voltaic materials in crucibles, which are usually square-shaped for a convenient and materialless effective wafer production. In the DS process, silicon ingots of different sizes are produced, which keep growing to fit the demand for solar cells. The quality and the price of such ingots depend primarily on the feedstock [2]. However, the success of each production step, two of which – melting and solidification – include the liquid phase, is also crucial for the cell quality parameters, i.e. poly-crystalline grain size, concentration of incorporation, dislocations, and other defects. Understanding and control of the melt flow during the solidification phase is important for the reduction of N, C and O incorporation and precipitation formation [3], [4], [5]. Small concentrations of SiO_2 precipitations can positively influence the output material, while SiC and Si_3N_4 decrease the efficiency of the solar cells dramatically and make the material brittle in the sawing process.

A number of investigations on the melt flow in DS-type crucibles is discussed in the literature. In model experiments, it is possible to satisfy the Reynolds number similarity criteria [6], but obtaining a similar buoyancy force to inertial force ratio requires very high temperature gradients for downscaled models [7]. Numerical simulation tools are also widely used [8, 9] to calculate the concentration distribution, the flow pattern and the solid-liquid interface shape. However, many aspects of turbulence are present in flows in the DS process, which have not been analyzed. The isotropic turbulence assumption is widely used without verification (e.g., in the k-ε model), but anisotropy is proven to be present in different flows, e.g., MHD turbulence [10].

In this work, a model experiment is reported, which allows obtaining reasonably higher buoyancy-to-inertial force ratios than previously reported in the literature. Large Eddy Simulation (LES) results for isothermal and stratified cases are presented, the isotropy of turbulence and the turbulent Prandtl number dependence on the vertical temperature gradient are discussed.

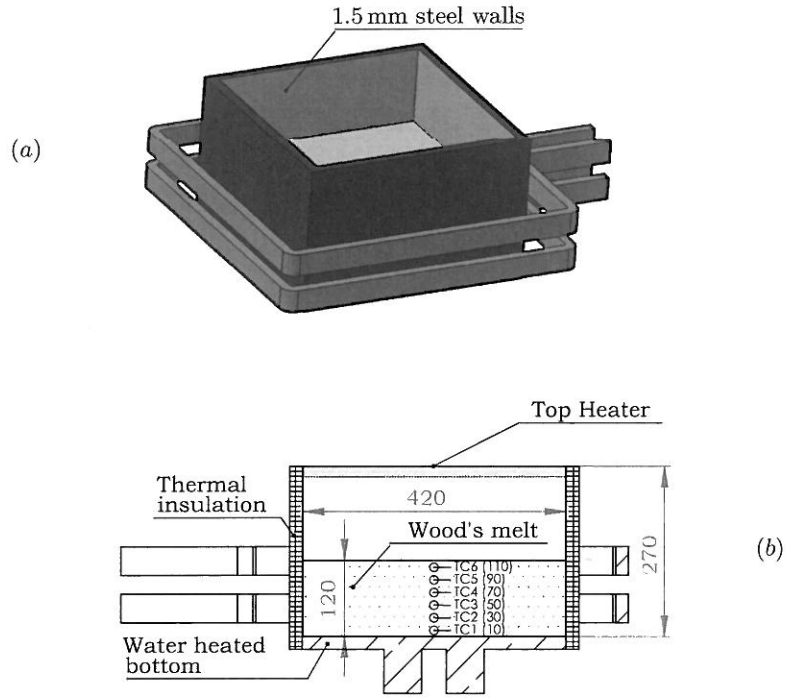

Fig. 1. Sketch of the experimental model: (*a*) isometric view of the experimental model; (*b*) middle cross-section of the experimental model, positions of thermocouples are showed as TC1...6. Side walls are isolated to reduce the horizontal temperature gradient.

1. Experimental model. Experimental results were obtained using a physical model (Fig. 1*a*), which consisted of a square-shaped steel crucible (wall thickness 1.5 mm), with the side length $W = 420$ mm and height $H = 270$ mm, filled to a level of $L = 120$ mm and placed on an aluminum plate with a constant temperature provided by a hot water ($T = 80°$C) flow. A Wood's alloy (50% Bi, 25% Pb, 12.5% Sn, 12.5% Cd, melting temperature 72°C) was used as a working liquid. The properties of the Wood's alloy if compared with the properties of silicon are listed in Table 1. The differences between both metals are within one order of magnitude, which allows using this alloy for a downscaled model.

The crucible is surrounded by two copper windings, which are one-phase-connected to a 50 Hz power supply. As both windings are connected to a bridge, the current can redistribute between them, but the current ratio between the top and bottom winding $I_{\text{top}}/I_{\text{bottom}}$ was approximately 1.08 for all cases. The maximum current was 3500 A with a total power up to 4 kW.

A radiation heater is used as a lid on the crucible, which allows obtaining a vertical temperature gradient in the alloy. The emissivity of the Wood's alloy is low ($\epsilon \sim 0.15$) and the radiation heating is not efficient to obtain high temperature gradients. However, a significant part of the heat flux on the free surface is ensured by the heated air in the space between the alloy and the lid. With the discussed setup, a steady temperature difference up to 80°C between the top and bottom surfaces was obtained in the melt at rest. The vertical temperature profile was measured using six thermocouples (TC); their vertical coordinates z (the bottom

Table 1. Liquid silicon and Wood's alloy physical properties.

Property	Silicon	Wood's Alloy	Ratio
Density ρ [kg/m^3]	2530	9400	3.72
Kinematic viscosity ν [m^2/s 10 ^{7}]	3.3	4.5	1.36
Heat conductivity λ [W/m K]	67.0	14.0	0.21
Heat capacity c [J/kg K]	990	168	0.17
Thermal expansion coefficient, β [1/K 10 ^{4}]	1.44	1.20	0.83
Electrical conductivity σ [S/m 10^6]	1.2	1.15	0.96

2. Numerical methods. The electromagnetic problem is described by the Maxwell system of equations and by the Ohms law. The number of variables in the system is reduced by using the potential approach, i.e. an electric vector potential $\mathbf{T}$ and a magnetic scalar potential Ω are introduced, leading to the so-called T-Ω formulation:

$$\mathbf{J} = \operatorname{rot} \mathbf{T},$$

$$\mathbf{H} = \mathbf{T} \quad \operatorname{grad} \Omega.$$

Using $\operatorname{div}\mathbf{B} = 0$ and $\operatorname{rot}\mathbf{E} = \quad \partial\mathbf{B}/\partial t$, the following equations are derived, which are numerically solved:

$$\frac{1}{\sigma} \operatorname{rot}\operatorname{rot}\mathbf{T} + i\omega\mu_0 (\mathbf{T} \quad \operatorname{grad}\Omega) = 0,$$

$$\operatorname{div}(\mathbf{T} \quad \operatorname{grad}\Omega) = 0.$$

This formulation is used instead of the more common A-V formulation because of a smaller number of variables in the non-conducting domains (air, insulators), which have the most finite elements in the calculation model. Electromagnetic (EM) simulations are performed with the GetDP general finite element solver. The EM calculation is done once, and the force density distribution is imported in a fluid dynamic simulation as the source. Force oscillations with a double magnetic field frequency are neglected. Inductive heating is negligibly small compared to the vertical heat flux in the system due to the low frequency used (50 Hz).

The incompressible flow is described by the Navier–Stokes equation in the dimensionless form

$$\frac{\partial \mathbf{u}}{\partial t} + (\mathbf{u}\operatorname{grad})\mathbf{u} = \quad \operatorname{grad} p + \frac{1}{\mathrm{Re}}\Delta\mathbf{u} + \frac{\mathrm{F}_0}{\mathrm{Re}^2}\mathbf{f} \quad \frac{\mathrm{Gr}}{\mathrm{Re}^2}\theta \cdot \mathbf{z}. \tag{1}$$

Here u is the dimensionless velocity, p is the dimensionless pressure, θ is the dimensionless temperature, Re is the Reynolds number, Gr is the Grashof number, F_0 is an electromagnetic forcing parameter, which is a dimensionless number giving the measure of the ratio of electromagnetic to viscous forces in the flow:

$$\mathrm{F}_0 = F_{\max}\frac{L^3}{\rho\nu^2}, \tag{2}$$

where $F_{\max}$ denotes a maximum force density in the melt volume, L is a characteristic length (the melt height is used), ν is the kinematic viscosity. To characterize the stratified flow, the Richardson number is frequently used:

$$\mathrm{Ri} = \frac{\mathrm{Gr}}{\mathrm{Re}^2} = \frac{\beta\Delta T g L}{U^2} = \frac{N^2}{(U/L)^2}, \tag{3}$$

$$N = \sqrt{\frac{g}{\rho_0}\frac{\mathrm{d}\rho}{\mathrm{d}z}} \approx \sqrt{\frac{g\beta\Delta T}{L}}. \tag{4}$$

The critical Richardson number $\mathrm{Ri}_{\mathrm{cr}}$ is a criterion for the transition between strong and weak mixing regimes. The strong mixing regime is similar to 3D turbulence with possible anisotropy of flow due to buoyancy forces. The weak regime, on the other hand, is inefficient in heat transport, thus leading to a growth of the turbulent Prandtl number Pr_{t} [11].

Thermal processes in the melt are described by the heat transfer equation:

$$\frac{\partial\theta}{\partial t} + (\mathbf{u}\,\mathrm{grad})\theta = \frac{1}{\mathrm{Pe}}\Delta\theta. \tag{5}$$

Here the Peclet number $\mathrm{Pe} = LU/\alpha$, α denotes thermal diffusivity. A constant temperature boundary condition was used at the bottom, the walls were treated as adiabatic. A convective type condition was used at the top surface.

The simulations of the fluid flow was performed with the OpenFOAM software, the forces and Joule heat sources from electromagnetic simulations were interpolated on a hydrodynamic mesh by means of first order interpolation.

The flow anisotropy was characterized by anisotropy coefficients [12] as

$$K_1 = 2\frac{\left\langle(\partial u_x/\partial x)^2\right\rangle}{\left\langle(\partial u_y/\partial x)^2\right\rangle} \qquad K_2 = 2\frac{\left\langle(\partial u_x/\partial x)^2\right\rangle}{\left\langle(\partial u_z/\partial x)^2\right\rangle},$$

$$K_3 = 2\frac{\left\langle(\partial u_y/\partial y)^2\right\rangle}{\left\langle(\partial u_x/\partial y)^2\right\rangle} \qquad K_4 = 2\frac{\left\langle(\partial u_y/\partial y)^2\right\rangle}{\left\langle(\partial u_z/\partial y)^2\right\rangle}.$$

Angle brackets indicate the volume average. All cases are scaled with respect to the coefficient $(\overline{K_1})$ in the A1 case (see Table 1):

$$\overline{K_1} = \frac{1}{\tau}\int_0^\tau K_1(t)\mathrm{d}t \approx 0.77. \tag{6}$$

Then the corresponding normalized coefficients are

$$K_i^* = \frac{K_i}{\overline{K_1}}. \tag{7}$$

Anisotropy of the energy-containing scales can also be characterized by a traceless anisotropy tensor defined by [13]

$$b_{i,j} = \frac{\langle u_i' u_j'\rangle}{\langle u_k' u_k'\rangle} \quad \frac{1}{3}\delta_{ij}. \tag{8}$$

It has two invariants: $II = b_{ij}b_{ji}$ and $III = b_{ij}b_{jk}b_{ki}$. II is positively defined and its value represents a degree of anisotropy. The sign III points out the nature of anisotropy – with a positive III, the flow tends to be "prolate" or "rod-like" (with one dominating component), while with a negative III, the flow is "oblate"

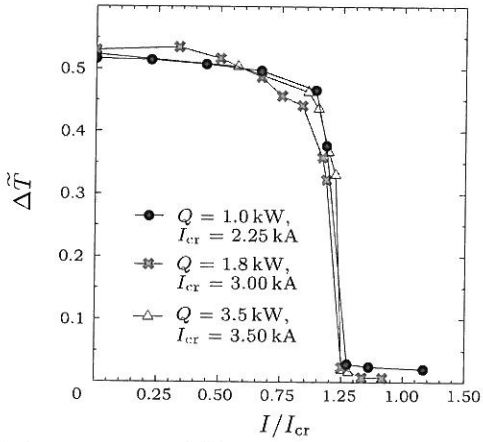

Fig. 2. Vertical temperature difference dependence on the current in windings.

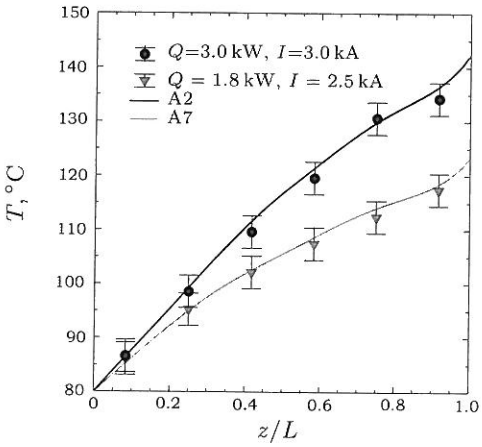

Fig. 3. Vertical temperature distribution in LES and in experiment.

3. Temperature measurements and model scaling. In the stratified flow, a damping of vertical mixing takes place. This phenomenon was observed experimentally: with a constant top heater power, the EM forcing was turned on with a different intensity (the current I in the windings) every time under the same initial conditions (fluid at rest, a fixed heater power Q). Fig. 2 shows a normalized vertical temperature difference $\Delta\widetilde{T} = (A\lambda\Delta T)/(LQ)$ (A is the surface area) dependence on the current I/I_{cr} in the windings. I_{cr} is a critical current, at which the Richardson number becomes smaller than unity and turbulent mixing dominates. It is shown in [14] that the critical Richardson number $\mathrm{Ri}_{cr} \sim 5 \ldots 10$, i.e. above unity, which is a typical threshold found in the literature. When the current reaches I_{cr}, the velocity-shear driven vertical turbulent motion is no longer damped by buoyancy forces, and the flow pattern changes from a stratified quasi two-dimensional, wave dominated pattern to a three dimensional, chaotic, strongly turbulent regime [11].

As the current goes to zero, the normalized temperature tends to an asymptotic value $\Delta\widetilde{T} \approx 0.5$. This value is explained by the fact that only half of the power from the heater passes through the melt in the vertical direction. The rest is losses through the lid and walls.

A comparison between vertical temperature distributions in experiment and simulations is shown in Fig. 3. Good agreement is achieved and it evidences that the use of the convective heat flux boundary condition is reasonable

Table 2. Parameters of LES simulations. I is the total current in both windings, T_{bot} is the bottom wall temperature (always 80°C), T_{top}, and h denotes the reference temperature and the heat transfer coefficient at the top surface. Simulations in A1 are performed with a reduced buoyancy effect: g was set to 10^{-3}.

Case	Current I, [kA]	T_{top}, [°C]	h, [W/m^{2}K]	Re	Ri
A1*	2.5	150	1400	10400	0.08
A2	3.0	150	1400	6133	17.1
A3	3.0	230	1000	5813	40.1
A4	4.2	150	1400	12373	3.0
A5	6.0	150	1400	24347	0.6
A6	2.1	150	1400	4027	40.9
A7	2.5	130	1400	5200	17.1
A8	2.5	150	1400	4827	28.0
A9	3.0	130	1400	6347	11.1

The results of this model experiment can be partly applicable to the silicon growth equipment with similar electromagnetic forcing. Scaling is performed for the generation 5 (G5) silicon growth furnace; the number 5 testifies the number of standard wafers (size 156×156 mm^2) obtained from a silicon ingot [15]. Relations for the velocity and average vertical temperature gradient G were calculated for the physical model and for the G5 silicon furnace: $U_{\text{G5}} = 0.37U_{\text{model}}$, $G_{\text{G5}} = 0.03G_{\text{model}}$. The highest temperature gradients, which can be obtained in this model, are $G = 750\,\text{K/m}$, which correspond to $G_{\text{G5}} = 22.5\,\text{K/m}$. Typical numbers for silicon furnaces are one order of magnitude higher.

4. LES results. LES were performed for different heating and EM forcing parameters. The simulation parameters are summarized in Table 2.

In the simulations, the boundary condition $q = h(T - T_0)$ was assumed on the free surface. The coefficient h was estimated from experimental observations by measuring the air temperature 1 mm above the free surface. The estimated heat transfer coefficient for the 2.0 kW heater power was $h_{\text{exp}} = 1500\,\text{Wm}^{-2}\text{K}^{-1}$. For the 3.5 kW power, $h_{\text{exp}} = 1360\,\text{Wm}^{-2}\text{K}^{-1}$. In the simulations, the h dependence on the heater power was neglected and the value $h = 1400\,\text{Wm}^{-2}\text{K}^{-1}$ was used.

The development of anisotropy was compared for four cases: small buoyancy effect (A1), intermediate Richardson number flow (A9 and A2) and stratified flow (A6). The results are presented in Fig. 4. For all cases with Ri $\gg 1$ (A2, A6, A9), the stratification changed the flow character, but the anisotropy coefficients K never differed from unity by more than 4 times. The strain-rate tensor components $S_{ij} = 1/2(\partial\overline{u_i}/\partial x_j + \partial\overline{u_j}/\partial x_i)$ are obviously within one order of magnitude for isothermal and stratified cases. A noticeable difference existed in a time required for the coefficients K to reach a steady value in all cases. The A1 case results (Fig. 4*a*) are almost constant in time, since the coefficients K reached their mean value already after 20τ ($\tau = L/U$). The intermediate Ri cases (A2 and A9 in Figs. 4*b*,*c*) required nearly 125τ to reach their end value, while the high Ri case (A6, Fig. 4*d*) needed less than 25τ. This is most likely related to the initial condition for temperature ($T = \text{const}$). The vertical temperature gradient developed from zero to a maximum value significantly slower than the velocity field (the Peclet number was large: Pe = Re Pr). A 3D flow pattern, which developed in all simulations at the initial time, was either slowly damped, while the temperature gradient was

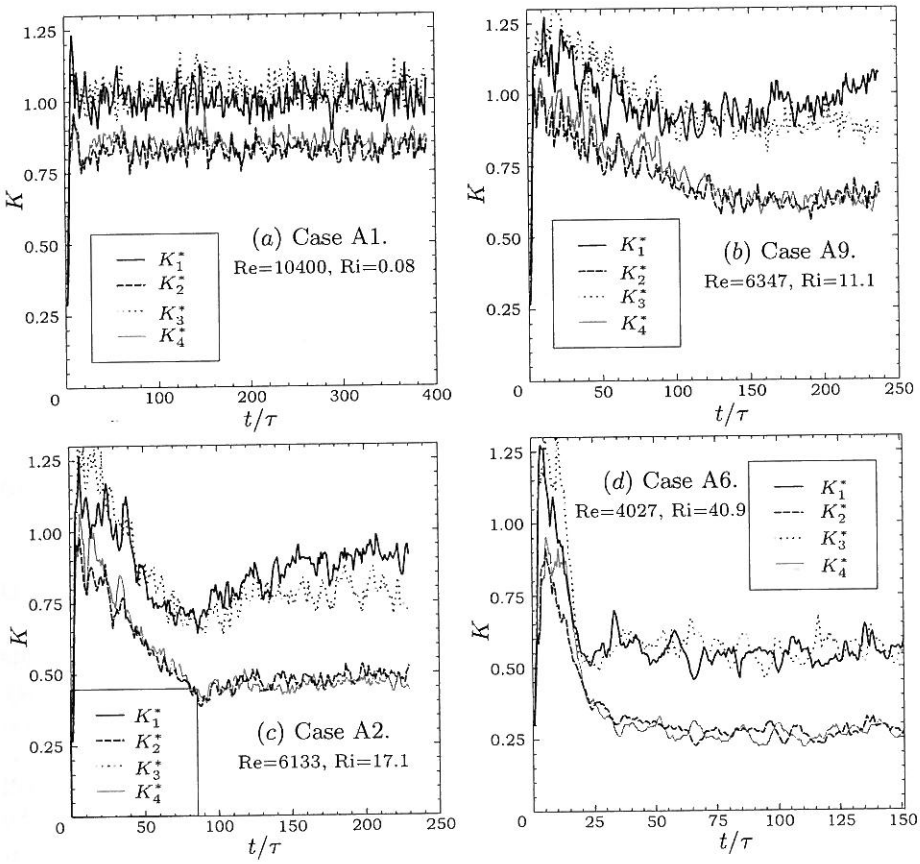

Fig. 4. Development of the anisotropy coefficients $K_{1\ 4}^*$ over the simulation time.

The coefficients K_2 and K_4, which both include a derivative of u_z, are always lower than K_1 and K_3. Since this effect is present also in a case, which is weakly influenced by buoyancy (A1, Fig. 4*a*), a possible cause could be the flattened geometry (the height/width ratio is ≈ 0.3), where the flow is more damped by the walls in the vertical direction than in horizontal.

For a more detailed analysis of the flow anisotropy, invariants of the $b_{i,j}$ (Eq. 8) tensor were used; the results are plotted in Fig. 5. Lumley [13] showed that invariants II and III were limited in their values, and the plane of these values forms a turbulence triangle; values outside of the triangle are not allowed. The (0,0) point corresponds to 3D turbulence; the leftmost point to isotropic 2D turbulence, and the rightmost point to 1D turbulence. The upper line of the triangle represents 2D turbulence, which by moving from left to right transforms from oblate to prolate.

The results obtained in LES at different time steps were plotted on this triangle for the cases A1-6. Three cases with the highest Richardson number have points in the most upper left corner of the turbulence triangle. A6 had the highest Ri and, therefore, the A6 data were placed in the most upper left position in the triangle. However, all these cases also had Reynolds numbers in the range 4000–6100, where the developed turbulence assumption may not be valid. The other cases had points closer to 3D turbulence. As shown in the experiment, transition

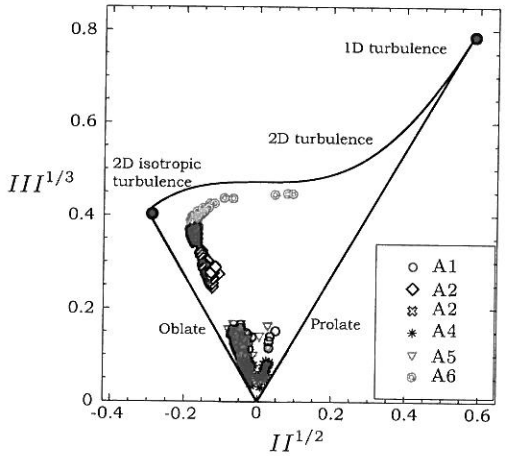

Fig. 5. LES results plotted on the turbulence triangle. The triangle form defined in [13].

cases within the strong mixing regime (A1 and A5) are further away from the 3D turbulence point than the A4 case.

The results of the $b_{i,j}$ invariants point to the anisotropy of the Reynolds stress tensor $\tau_{ij} = \rho\overline{u_i'u_j'}$ for strongly stratified flows. The widely used eddy viscosity assumption ($\tau_{ij} = 2\mu_t S_{ij}$) based models might, therefore, experience difficulties capturing effects existing in the stratified flow. Several anisotropic eddy-viscosity assumption based models have been developed [16], however, they still require an adjustment of constants. One of the most important constants in the turbulent heat transfer calculation is the turbulent Prandtl number $\mathrm{Pr_t} = \nu_t/\alpha_t$. Typical values used for turbulent flows vary between 0.7 and 1.0. However, it was shown that the turbulent Prandtl number depended on the local temperature gradient [17].

In LES, the volume averaged $\mathrm{Pr_t}$ and Ri were obtained for sub-volumes: the calculation domain was split in 10×10 blocks along the x- and y-directions, respectively. To separate vertical mixing from horizontal, the turbulent Prandtl number was calculated as

$$\mathrm{Pr_t} = \frac{\overline{u_h'u_z'}}{2S_{hz}}\frac{\partial\overline{T}/\partial z}{\overline{u_z'T'}}.$$

Here the index h corresponds to the horizontal velocity $u_h = (u_x^2 + u_y^2)^{1/2}$. These data and the fitting curve are plotted in Fig. 6. From theoretical considerations in [17], it is known that the Prandtl number is a linear function of the Richardson number at high Ri.

Fitting was performed using the logarithmic least squares method, and the obtained curve is $0.76 + 3.17\,\mathrm{Ri}$. $\mathrm{Pr_{t0}} = 0.76$ is close to the typical values for turbulent flows as well as the curve slope (3.17). Values found in the literature are 4.0 [17], 5.0 in [11], 2.0 in [18]. The linear curve is used since it gives the best agreement for the whole Richardson number range – the Prandtl number is equal to $\mathrm{Pr_{t0}}$ at a very small Ri (neutral conditions) and theoretically proven constant slope as $\mathrm{Ri} \to \infty$. However, the linear function does not give a good approximation of the weakly stable stratification regime – $\mathrm{Ri} = 0.1 \ldots 1.0$, where different functions are used to fit the Prandtl number [18, 19].

The dashed line in Fig. 6 represents the constant flux Richardson number $\mathrm{Ri_f}$:

$$\mathrm{Ri_f} = \frac{\mathrm{Ri}}{\mathrm{Pr_t}} = \frac{g\beta\overline{u_z'T'}}{\tau S}.$$

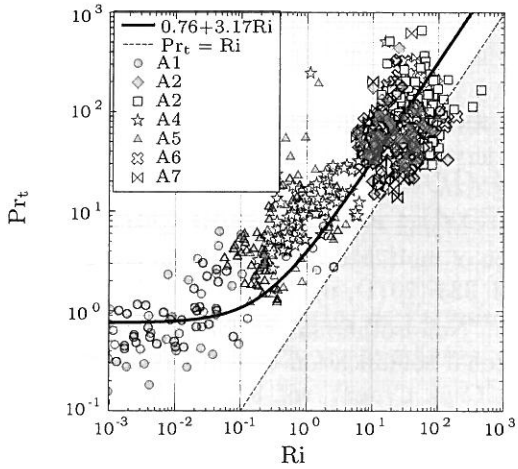

Fig. 6. $\mathrm{Pr_t}$ as a function of *Ri* in LES for different cases.

The numerator here represents the turbulence dissipation by buoyancy and the denominator the turbulence generation by shear, therefore, $\mathrm{Ri_f}$ cannot exceed unity. In the discussed results (Fig. 6), there are certain points in the high-Ri flow regimes, where $\mathrm{Ri_f}$ locally exceeds unity. The local exceeding of this threshold can be explained by the non-uniform turbulence generation, which is then transported by convection to zones with the high temperature gradient and buoyant dissipation.

5. Conclusions. The experimental results evidence that in a directional solidification system there is a transition between two-dimensional weak mixing and three-dimensional strong mixing regimes at the Richardson numbers $\sim 5 \ldots 10$. The experimental results also were used to estimate the heat transfer coefficient for the convective boundary condition in LES.

LES has shown that turbulence is not isotropic when the Richardson number is large and the vertical turbulent heat transfer decreases as Ri grows. The turbulent Prandtl number dependence on the Richardson number is obtained and compared with numbers given in the literature; a good agreement is achieved. This aspect of turbulence is important for a correct vertical heat transfer estimation and should be taken into account in RANS turbulence models.

LES results also show that the turbulence character is disk-like and it gets closer to 2D isotropic turbulence as the Richardson number increases.

Acknowledgements. This research was partly supported by the European Social Fund project No. 2013/0027/1DP/1.1.1.2.0/13/APIA/VIAA/007.

REFERENCES

[1] H. Wirth. *Aktuelle fakten zur photovoltaik in deutschland* (2014) (in German).

[2] G. del Coso, C. del Cinizo, and W. Sinke. The impact of silicon feedstock on the pv module cost. *Solar Energy Materials and Solar Cells*, vol. 94 (2010), pp. 345–349.

[3] C. Reimann, *et al.* Modeling of incorporation of o, n, c and formation of related precipitates during directional solidification of silicon under consid-

[4] H. Moller, L. Long, M. Werner, and D. Yang. Oxygen and carbon precipitation in multicrystalline solar silicon. *Phys. Stat. Sol.*, vol. 171 (1999), pp. 175–189.

[5] G. Du, N. Chen, and P. Rossetto. On-wafer investigation of sic and si3n4 inclusions in multicrystalline si grown by directional solidificatione. *Sol. Energy Mater. Sol. Cells.*, vol. 92 (2008), p. 1059.

[6] K. Dadzis, *et al.* Model experiments and numerical simulations for directional solidification of multicrystalline silicon in a traveling magnetic field. *J. Crys. Growth*, vol. 333 (2011), pp. 7–15.

[7] K. Dadzis, *et al.* Non-isothermal model experiments and numerical simulations for directional solidification of multicrystalline silicon in a traveling magnetic field. *J. Crys. Growth*, vol. 372 (2013), pp. 1454–156.

[8] Y. Tenga, J. Chen, B. Huang, and C. Chang. Numerical simulation of impurity transport under the effect of a gas flow guidance device during the growth of multicrystalline silicon ingots by the directional solidification process. *J. Crys. Growth*, vol. 385 (2014), pp. 1–8.

[9] N. Dropka, W. Miller, R. Menzel, and U. Rehse. Numerical study on transport phenomena in a directional solidification process in the presence of travelling magnetic fields. *J. Crys. Growth*, vol. 312 (2010), pp. 1407–1410.

[10] O. Zikanov and A. Thess. Direct numerical simulation as a tool for understanding mhd liquid metal turbulence. *Solar Energy Materials and Solar Cells*, vol. 28 (2004), pp. 1–13.

[11] S.S.. Zilintikevich, *et al.* Turbulence energetics in stably stratified geophysical flows: Strong and weak mixing regimes. *Q. J. R. Meteorol. Soc.*, vol. 134 (2008), pp. 793–799.

[12] W.D. Smith and J.N. Moun. Anisotropy of turbulence in stably stratified mixing layers. *Phys. Fluids*, vol. 12 (2000), pp. 1343–1362.

[13] J. Lumley and G. Newmans. The return to isotropy of homogeneous turbulence. *J. Fluid Mech.*, vol. 81 (1977), pp. 161–178.

[14] V. Geza, B. Nacke, E. Baake, and A. Jakovics. Influence of the richardson number on em force driven flow structures in square-shaped crucible. *J. Crys. Growth*, vol. 401 (2014), pp. 895–898.

[15] C. Kudla, *et al.* Crystallization of 640 kg mc-silicon ingots under traveling magnetic field by using a heater-magnet module. *Journal of Crystal Growth*, vol. 365 (2013), no. 0, pp. 54 – 58.

[16] S.M. Murman. A scalar anisotropy model for turbulent eddy viscosity. *International Journal of Heat and Fluid Flow*, vol. 42 (2013), pp. 115–130.

[17] S.K. Venayagamoorthy and D.D. Stretch. On the turbulent prandtl number in homogeneous stably stratified turbulence. *J. Fluid Mech.*, vol. 644 (2010), pp. 359–369.

[18] S. Sukoriansky, B. Galperin, and I. Staroselsky. A quasinormal scale elimination model of turbulent flows with stable stratification. *Physics of Fluids*, vol. 17 (2005), p. 085107.

[19] P.S. Anderson. Measurement of prandtl number as a function of richardson number avoiding self-correlation. *Boundary-Layer Meteorol*, vol. 131 (2009), pp. 345–362.